Performance Estimation of a Real-Time Rosette Imager

Gene Stoltz[a, b] and Marnus Stoltz[c]

[a]University of Johannesburg, South Africa
[b]Council for Scientific and Industrial Research of South Africa
[c]University of Otago, New Zealand

ABSTRACT

In this paper, we model a real-time feasible rosette imager, consisting of a rosette scanner, an optical sensor and a deterministic image reconstruction algorithm. We fine-tune the rosette imager through selecting the appropriate sensor field of view and rosette pattern. The sensor field of view is determined through a greedy approach using uniform random sampling. Furthermore, the optimal rosette pattern is selected by determining which pattern best covers the imaging area uniformly.

We explore image sparsity, image decimation and Gaussian filtering in a well-known natural data set and dead leaves data set using the PSNR, Peak-Signal-to-Noise Ratio. This exploration helps to establish a connection between PSNR and image sparsity. Furthermore, we compare various rosette imager configurations in a Bayesian framework. We also conclude that the rosette imager does not outperform a focal-plane array of equivalent samples in terms of image quality but can match the performance.

Keywords: Image Formation, Compressed Sensing, Rosette Scanning Systems.

1. INTRODUCTION

Infrared imaging is a key sensing component in support of digital technologies. Development of infrared imaging have shifted focus from scanning single detectors to focal-plane arrays, driven mostly by advances in manufacturing technology.[1] Single detector scanning systems lack the quality and resolution of current focal-plane array systems and require advanced sampling strategies and higher data processing. The improvement of computational capability and development of new sampling theories, such as compressed sensing,[2] has provided new opportunities for imaging through single detector scanning systems such as the rosette scanner.

It was shown that an infrared rosette scanner with a single detector, equivalent to an infrared seeker system, can produce images offline via compressed sensing.[3] The image formation process through compressed sensing was further improved by modelling detector measurements as the sum of multiple pixels, replacing the binary orthonormal measurement matrix first used[4].[5] Recent attempts to improve image reconstruction quality either combines multiple frames[6] or smaller image blocks.[7] Here we design a real-time imaging device using a single detector scanning system that match the performance of focal-plane arrays.

The paper is structured as follow: In Section 2 we introduce the rosette imager and a performance optimisation process. Then, in Section 3, we discuss the methods used and experimental protocols followed for evaluating the optimised imager. The discussion includes a description of the testing data sets, Peak-Signal-to-Noise Ratio(PSNR) as performance measure and the importance of image sparsity for parameter inference. Thereafter, in Section 4, we discuss performance results of the rosette imager based on four rosette patterns and a focal-plane array. Lastly, in Section 5, we discuss future work and give some concluding remarks.

Further author information: (Send correspondence to G.Stoltz)
G.Stoltz: E-mail: ggsgene@gmail.com

2. THE ROSETTE IMAGER

The rosette imager is defined by the rosette scanning pattern and a compressed sensing setup. Briefly, the rosette scanning pattern is the sampling pattern produced by the mechanical movement of an actual imager. The compressed sensing setup is how the samples are reconstructed to represent the image that was sampled. We discuss these two components in more detail below. The requirements for the rosette imager being designed is as follow:

- An output image with resolution of 256×256 pixels.

- A frame rate of 25 frames per second (fps).

- Real-time performance, subjected to a latency of 2 frames or 80 ms.

The designed imager must be practical and therefore the physical realisation can be achieved through utilising a rosette scanner. The rosette scanner has multiple parameters that can be adjusted to achieve different optimisations. For example, sensor sensitivity in relation to integration times can be improved by using slower rotation frequencies and lower sampling rates.[8]

In this paper only the rosette scanning pattern and the detector field of view will be optimised for best image quality. It must be noted that all physical effects, such as lens distortion, mechanical precision, sensor noise and integration times, are ignored in the system evaluation.

2.1 The Rosette Scanning Pattern

The rosette scanning pattern can be realised by using a combination of rotating canted mirrors, optic wedges or canted rotating detector. The paper will use a wedge typed rosette scanner as shown in Figure 1. The rosette scanner must satisfy certain condition to successfully form a scanning pattern. The scanning pattern is presented by the locus that the Instantaneous Field of View (IFOV) will travel when projected onto a plane perpendicular to the rotation axis (See Appendix A.1 for governing equations). The different rosette scanning patterns are denoted by two integer values (n, m).

(a) Physical Layout
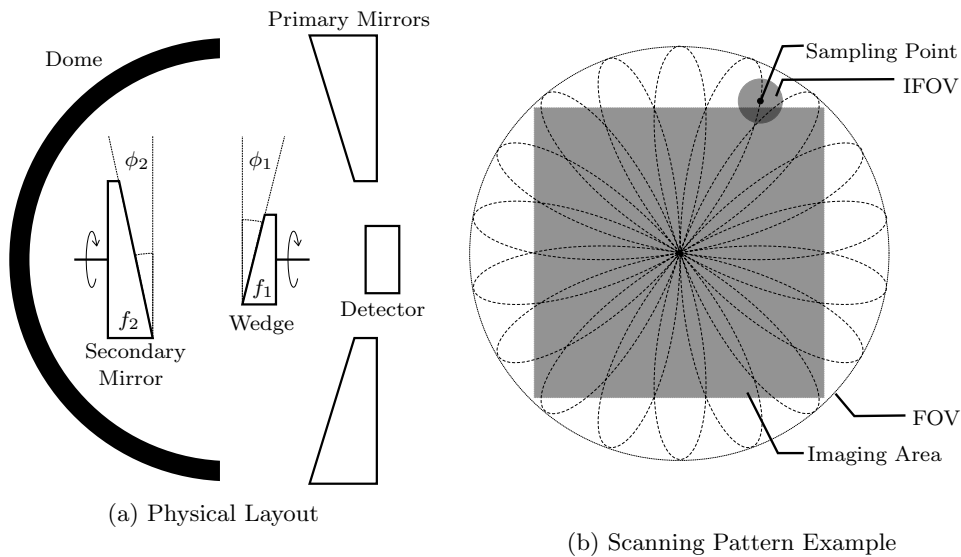
(b) Scanning Pattern Example

Figure 1: The Rosette Scanner. A wedge typed scanner is demonstrated in Figure 1a. A typical scanning pattern with frequency $f_1 = 100Hz$ and $f_2 = -175Hz$ (n,m = 11,4) is shown in Figure 1b. The system's Field of View (FOV) is the total area covered by the rosette scanner. The Instantaneous Field of View (IFOV) is the field the sensor covers while the sampling point indicates the optical axes of the detector.

The physical realisation of a rosette scanner have various processes that impose limitations such as manufacturing quality and cost. The following limitations can be imposed on the rosette scanner parameters used for the design of the rosette imager.

- The rotational frequency of the mirror and wedge is limited to 2500 Hz.

- The maximum sampling frequency of the detector is limited to 510 kHz.

2.2 The Compressed Sensing Setup

The compressed sensing setup consist of a measurement and reconstruction matrix .[9] The measurement matrix is governed by the limitations of the rosette scanner while the reconstruction matrix, generated by the reconstruction algorithm, governs the speed of image formation and image quality.

The measurement matrix represents the detector output as a sum of pixel intensity values related to the output image.[5] The sample positions within the rosette pattern is discretised such that the optical axis of the detector is always in the middle of a pixel within the output image. The IFOV is dicretized in-terms of the output image and can be measured in pixel size. An example of a discretized detector is shown in Figure 2. The discretized IFOV is placed on the sample position of the rosette pattern. The generated image is flattened and coincide with a row entry in the measurement matrix. For every sample in the rosette scanning pattern a row is added into the measurement matrix. It must be noted that the image formation process assumes a discrete world where the mapping from a continuous to a discrete domain has not been taken into account. The reference to the IFOV might be misleading when talking about the imaging domain, thus it will rather be referred to as the probe size.
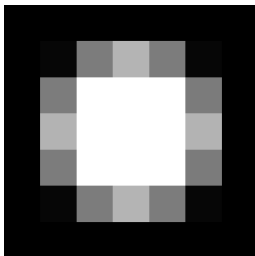

Figure 2: A probe with a radius of 2 pixels, starting in the middle of pixel (4, 4). The white pixels indicate a 1 and the black pixels indicate a 0 with the fractional values of the circle indicated by the grey values.

The reconstruction matrix is based on the chosen image reconstruction algorithm. The choice of reconstruction algorithm should allow for real-time execution while maintaining appropriate quality. A fair amount of reconstruction algorithms exist such as Basis Pursuit Denoising (BPDN)[10] and total variation regularisation (NESTA). Unfortunately, these algorithms are not suitable for real-time applications. A good candidate is the Fourier Domain Regularisation Inversion (FDRI) algorithm developed in 2018 by Czajkowski et al and has equivalent performance to NESTA.[11] The FDRI algorithm is based on the calculation of the Moore-Penrose pseudoinverse. The FDRI is not an iterative algorithm and allow reconstruction by performing a single matrix multiplication with a predetermined reconstruction matrix. The reconstruction matrix can be calculated before the execution of imaging, but require the knowledge of a known measurement matrix. In case of a rosette scanning pattern, the measurement matrix is known beforehand. It is important to note that FDRI is not an $l1$-regularisation algorithm but approximate the effects.

The real-time expectation of using the FDRI reconstruction matrix can be calculated by assuming an output image of 256×256 with 20% samples. The reconstruction matrix of size 65536×13107 can be multiplied by the measurement vector of size 13107 within $20ms$ utilising a GPU. (Tested on a nVidia GeForce 1060). The estimated speed of the execution makes the reconstruction algorithm real-time in-terms of the expected frame rate.

2.3 Design Optimisations

The rosette imager can now be designed through the optimisation of the probe size and the rosette scanning pattern. The probe size and sample positions have direct influence on the constructed measurement matrix and influencing the coherence between the measurement and reconstruction matrices. Although, the application of compressed sensing theory is limited by the fact that the probe samples in the spatial domain which is equivalent to the output domain. Despite this, compressed sensing principles will still be applied and random uniform sampling would be assumed to provide optimal reconstruction possibility.

To find the optimal probe size, a greedy approach is followed. The probe size and the percentage samples are linearly scanned while measuring the average PSNR over the dead leaves data set. For every probe size and sample percentage a set of random coordinates are uniformly distributed across the image. The number of generated coordinates in the set coincide with the sample percentage. The results of the greedy approach is shown in Figure 3a.

Interpreting the results it can be concluded that a small probe, provide a higher maximum PSNR but require a higher percentage of samples. For a certain sampling percentage there exist an optimal probe size which will produce the maximum possible PSNR performance while applying uniform random sampling. Combining the compressed sensing theory and evidence from these experimental results the optimal performance can be achieved by minimising the number of pixels not part of a sampled probe and minimising the amount of probe overlap.

The rosette imager design will have a single sample percentage and probe size. The sample percentage can be estimated by assuming the samples within the field of view of the rosette scanning pattern are uniformly distributed. A square within a circle will consist of approximately 63.6% of the circle area. A detector sampling at 510kHz will produce 20400 samples per 40 ms, thus 20400 samples per rosette scanning pattern at 25fps. Approximately 12974 samples will fall within the imaging area and with an output image 256×256 a sample percentage of 19.7% will be achieved. Figure 3b provides the result related to 19.7% sampling and produces probe size of 2.25 pixels at the maximum PSNR.
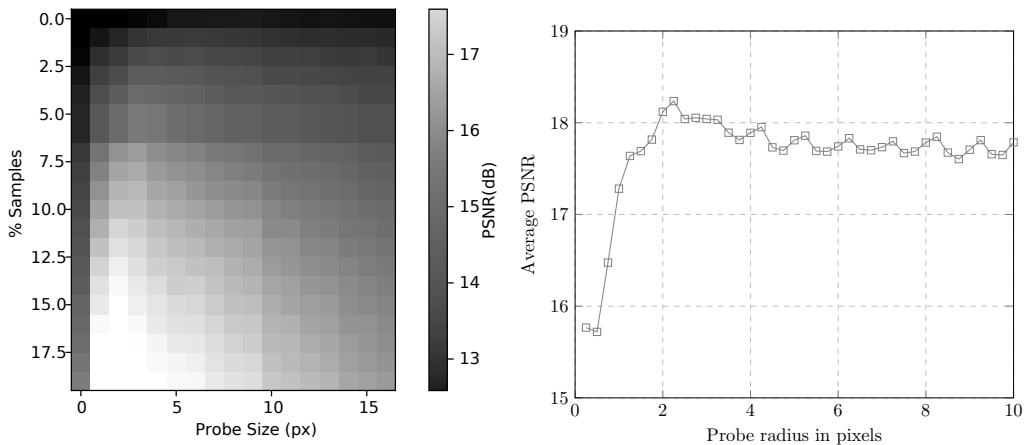
(a) The percentage samples versus probe size with grey values indicating the relative PSNR values.

(b) PSNR versus probe size for 19.7% samples. A probe size of 2.25 pixels provided the maximum PSNR value.

Figure 3: The result summary for the probe size optimisation process.

In order to find the optimal scanning pattern we set a criteria based on minimal probes overlap and maximal number of pixels scanned within the imaging area. The probe overlap was already minimised by selecting the optimal probe size. To determine the optimal scanning pattern a 2-dimensional histogram is constructed using the pixels as bins and filling the bins with the probe positioned by the selected rosette pattern. The number of non-zero bins are counted while the pattern producing the most non-zero pixels are assumed to cover the imaging area uniformly. The rosette scanner parameters (n, m) are linearly searched from $0 - 1000$ with the amount of

non-zero entries plotted in Figure 4c. The maximum value of the non-zero entries was measured and all entries equal to the maximum are plotted in Figure 4d (m and n only range from 0-100 for display purposes).
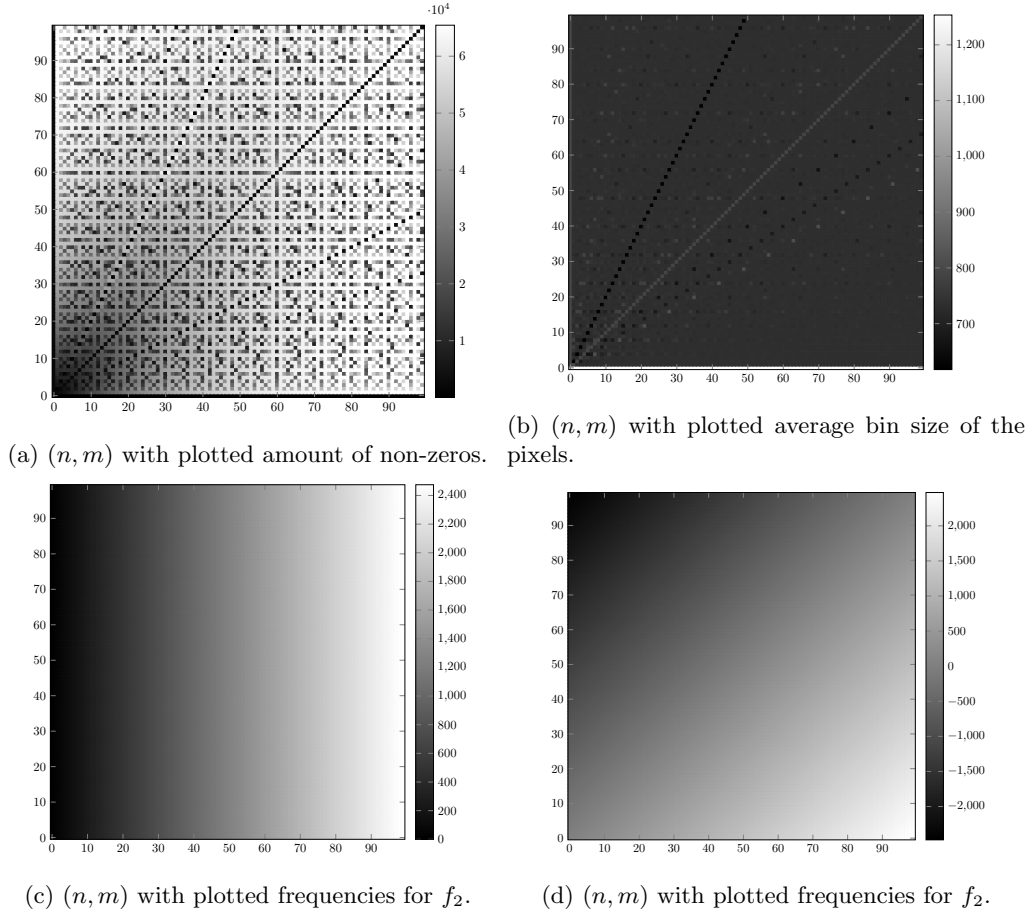

(a) (n, m) with plotted amount of non-zeros.

(b) (n, m) with plotted average bin size of the pixels.

(c) (n, m) with plotted frequencies for f_2.

(d) (n, m) with plotted frequencies for f_2.

Figure 4: Optimisation Images

From the million n,m-values (1000×1000) 1150 (m, n) combinations provided equivalent global maximum values of non-zero elements. The values were further filtered by (n, m) combinations providing rotational frequencies below 2500 Hz and 1000 Hz. The top three patterns for each filter are shown in Table 1 and Table 2.

Table 1: Top 3 rosette pattern producing most non-zero value with rotation frequencies less than 2500 Hz

non-zeros	n	m	Frequency 1	Frequency 2	Number of Samples
65450	8	99	2475	2275	11966
65428	15	98	2450	2075	11977
65444	20	97	2425	1925	11976

Table 2: Top 3 rosette pattern producing most non-zero value with rotation frequencies less than 1000 Hz

non-zeros	n	m	Frequency 1	Frequency 2	Number of Samples
64383	76	37	925	-975	12008
64377	76	39	975	-925	12009
63877	72	35	825	-925	11946

Figure 5 provide an illustration of the best 2500 Hz and 1000 Hz pattern with their respective histograms with probe size equal to 2.25 pixels. The pattern shown in Figure 5c is the pattern used for most previous

publications with $f1 = 100Hz$ and $f2 = -175Hz$. The probe size was adjusted such that the probe cover all pixels, equivalent to selecting the optimal IFOV for an infrared seeker system. The radius was found to be 31 pixels. The recommended sampling patterns for 2500 Hz are (8, 99) and for 1000 Hz are (76, 37) with a probe size of 2.25 pixels respectively.
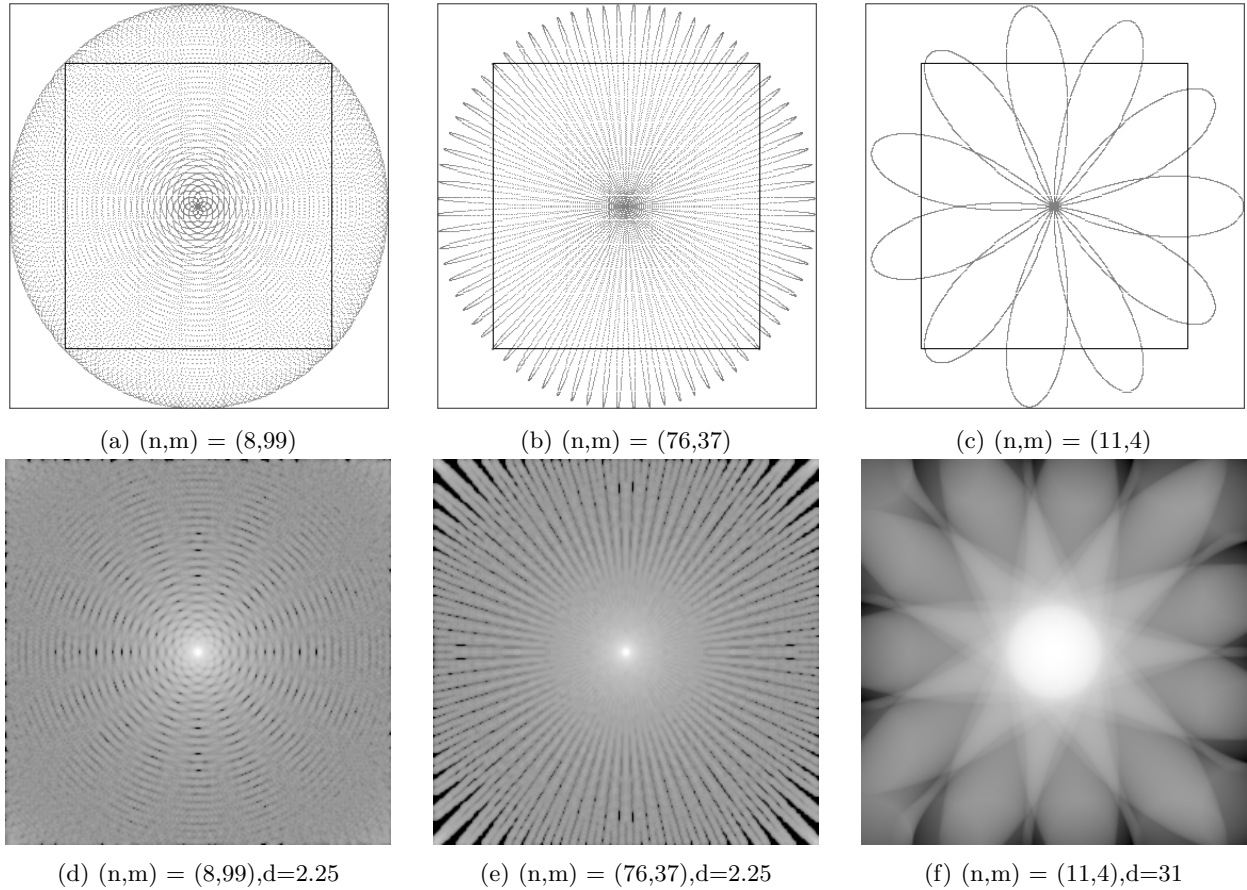

| (a) (n,m) = (8,99) | (b) (n,m) = (76,37) | (c) (n,m) = (11,4) |

| (d) (n,m) = (8,99),d=2.25 | (e) (n,m) = (76,37),d=2.25 | (f) (n,m) = (11,4),d=31 |

Figure 5: Illustration of the optimal sampling patterns with limiting frequencies

3. ASSESSMENT METHODS AND PROTOCOL

3.1 Data Sets

In the assessment of the rosette imager we used two datasets namely, the dead leaves dataset and the natural scene dataset. The deadleaves dataset is significant due to its scale invariance. Lee et el[12] introduced a scale invariance case of the general dead leaves model. This scale invariant case occurs when the power law distribution parameter of the simulation is set to 3. The scale invariant case of the dead leaves model approximate natural scenes when a small size cut-off on the circle radius's are introduced.[13] Perfect simulation of the stochastic geometry occurs[14] when backwards construction of the pattern is performed successfully simulating such an image. Generated dead leaves image samples are shown in Figure 6.

The natural scene data set is divided into various categories[15] such as forest, coast, mountains and open country. Examples are given in Figure 7.

3.2 Peak-Signal-to-Noise Ratio

Reconstructed images from the data sets (described above) are assessed based on the Peak-Signal-to-Noise Ratio (PSNR) measure. The PSNR measure is the inverse logarithm of the Mean Square Error between two
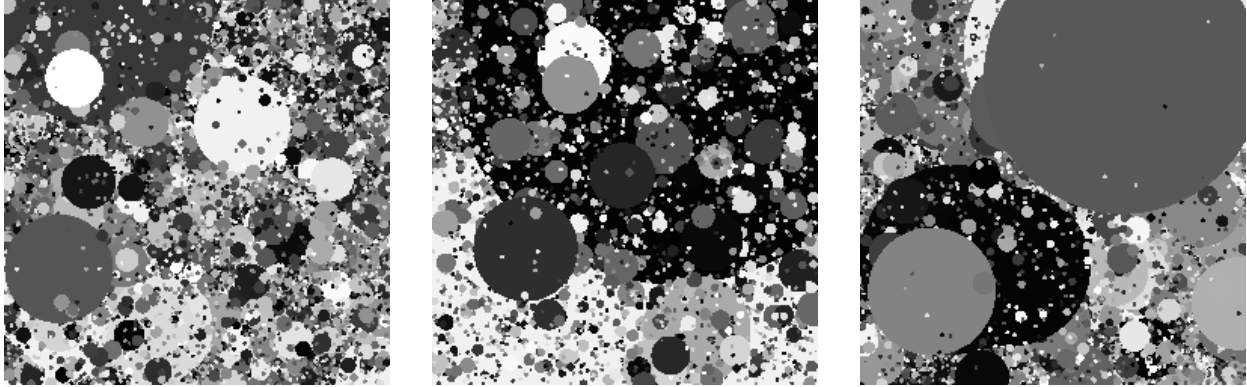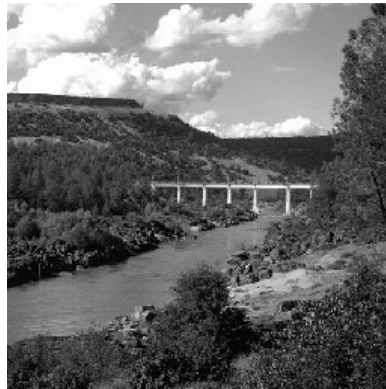
Figure 6: Dead leaves data set image examples.

(a) Forest   (b) Open Country   (c) Coast

Figure 7: Natural scene imaging examples

discrete valued images (See Appendix A.2). Images are converted to 16 bit, before measuring the PSNR, placing the maximum PSNR value at 96.33 dB. It is common to use the Structural Similarity(SSIM)[16] measure when comparing images although it is interesting to note that SSIM is related to PSNR.[17–19] It can be argued that according to some research papers SSIM is a better metric compared to PSNR or MSE. Not SSIM or PSNR can be used as a norm and is thus not an adequate measurement for vector spaces although MSE can be calculated from PSNR. SSIM might indicate the likelihood that the human visual system would find certain images more visually pleasing but this is not the purpose of a sampling system. The purpose is to accurately reconstruct a sampled signal and measure the accuracy. Therefore the PSNR measure is adopted and is also proposed for future research.

3.3 Image Sparsity

In compressed sensing one of the factors determining the quality of signal reconstruction is the sparsity of the signal itself. A more sparse signal will require fewer samples to reconstruct at a higher accuracy. The expected PSNR values should reflect this effect and is explored in Section 3.3.1 using the Discrete Cosine Transform (DCT). Also in the section, the large histogram variances on the PSNR values assert the requirement for advanced statistical techniques and the dead leaves data set is shown to be adequate evaluation set for comparing imaging algorithms.

Following on image sparsity in the DCT, an image with a fair amount of detail should reconstruct worse than an image with less detail. The dead leaves data set is generated to represent a highly detailed natural image, while the natural scene database consist of landscapes (low detail), mountain areas (medium detail) and forests(high detail). In Section 3.3.2 image sparsity is related to image detail.

3.3.1 Image sparsity in the Discrete Cosine Transform

The sparsity of an image is measured in accordance to a specific transformation basis. The Discrete Cosine Transform (DCT) will be used as the sparsity basis. The image sparsity is taken as the percentage of non-zero coefficients within the transform. Sparse images was created by selecting a percentage of the highest coefficients in the transform, setting all other coefficients to zero and taking the inverse transform. The number of coefficients required to reproduce an image at maximum PSNR value indicates the sparsity of the image.

The PSNR was calculated between the generated sparse image and the original image in the data set. Example images at different sparsity is shown in Figure 8 and Figure 9. The sparsity performance graphs for each data set is shown in Figure 10 with the histogram distribution for each sparsity level overlaid. In the figure it is clear that the Dead leaves data set persistently ranges at the bottom of performance of the natural scene data set and is, therefore, less sparse on average.
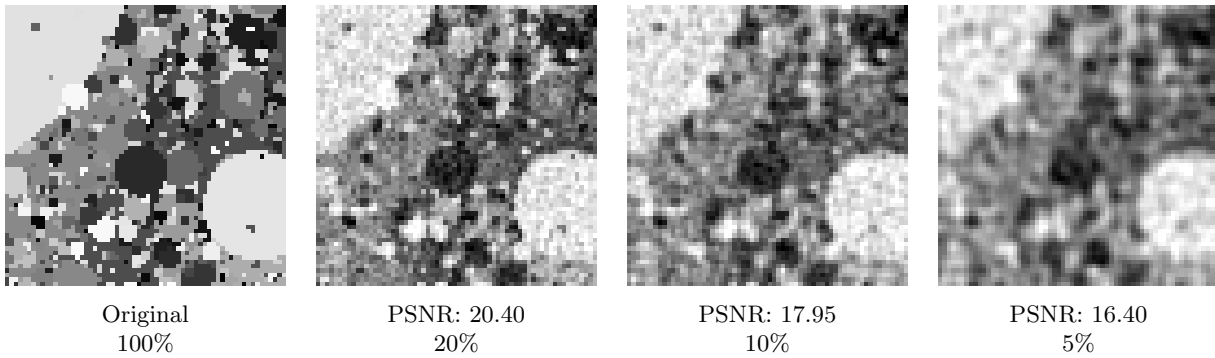

| Original | PSNR: 20.40 | PSNR: 17.95 | PSNR: 16.40 |
| 100% | 20% | 10% | 5% |

Figure 8: An example image from the dead leaves database reconstructed at different sparsity percentages based on the Discrete Cosine Transform

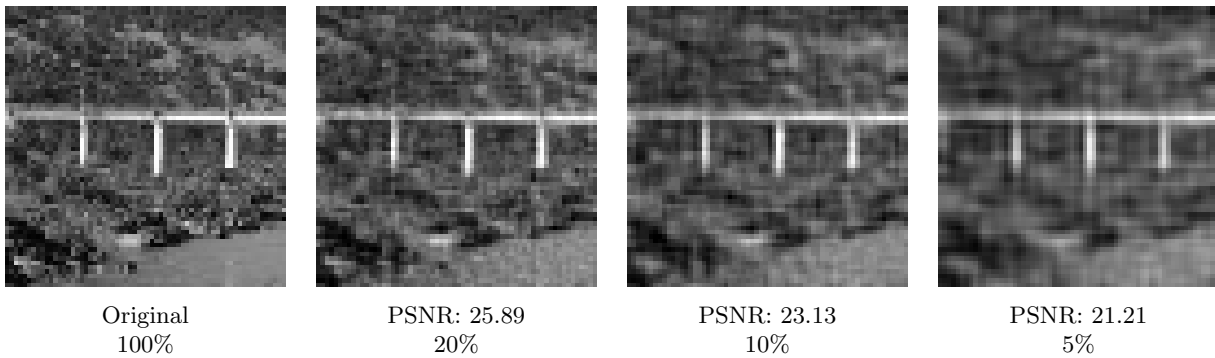| Original | PSNR: 25.89 | PSNR: 23.13 | PSNR: 21.21 |
| 100% | 20% | 10% | 5% |

Figure 9: Example image from the Scene database reconstructed at different sparsity percentages based on the Discrete Cosine Transform. The images was zoomed (128×128) to allow for closer investigation.

In Figure 11 a single PSNR histogram is shown for 50% sparsity from which it is clear that the Dead leaves data set covers the bottom part of the Natural Scene database. A worse PSNR value for the same amount of sparse coefficients indicate that the specific image is less sparse than another. Using this concept the various categories in the natural scene data set and the dead leaves data set can be plotted in a Figure 11c. The distribution created indicate the various sparsity categories. It is observed that the forest category achieve almost equivalent performance to the dead leaves category where the landscape categories outperform the average PSNR of the dead leaves significantly. This can be attributed to the sparseness found in the various categories and can be evaluated intuitively by comparing the detail in a forest-like image and the detail in an ocean view. It can be concluded that the dead leaves data set will provide a worst case performance and should be adequate to compare various algorithms without using full natural scene data sets.
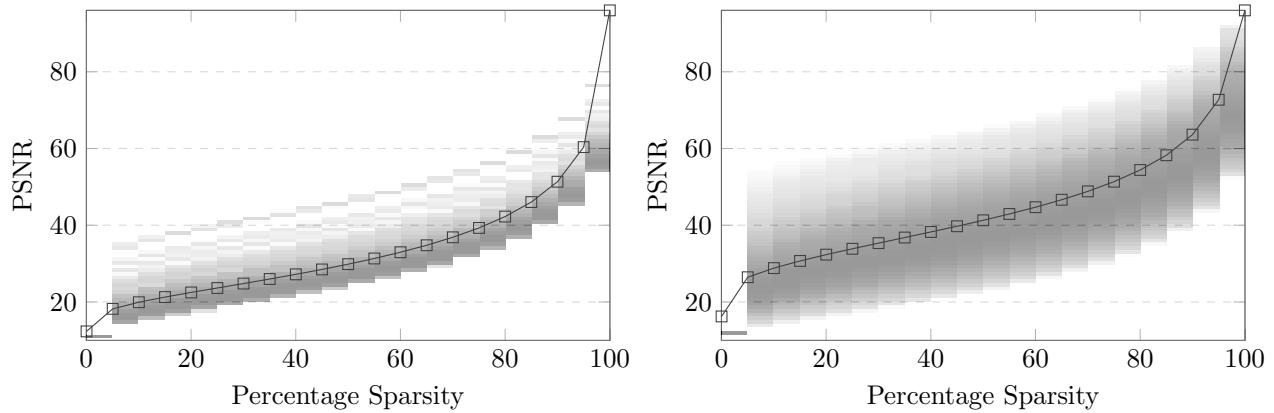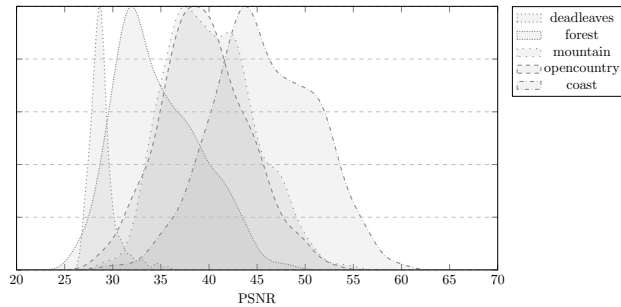
(a) Dead leaves data set

(b) Natural scene data set

Figure 10: Sparse image reconstruction in the Discrete Cosine Transforms with the average PSNR plotted and the PSNR histograms overlaid on the graph as a grey scale image for each different sparsity percentage.
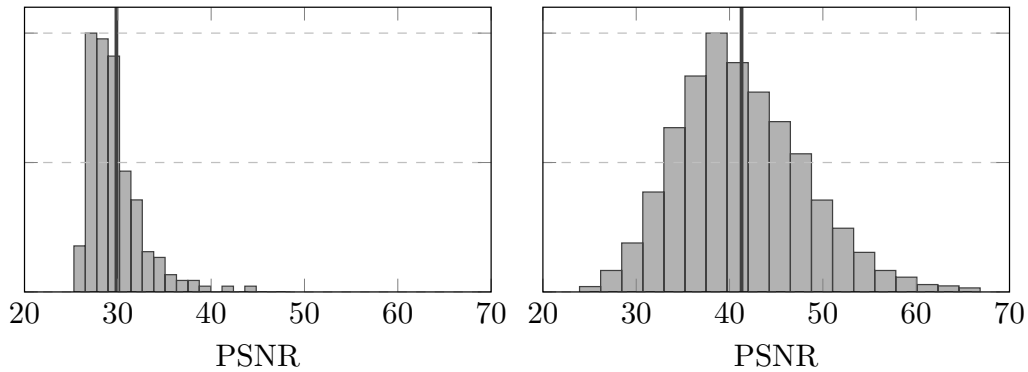
(a) Dead leaves data set

(b) Natural scene data set

(c) Normalised Distributions of different categories indicating difference in image sparsity.

Figure 11: The histogram of PSNR values for all images in each respective data set at a 50% sparsity reconstruction using the Discrete Cosine Transforms

3.3.2 Sparsity in a focal-plane array

In imaging and optics it is common practise to use the spatial frequency response (SFR) as an indication to how much detail can be observed in an image. The degradation of an image based on the SFR is commonly modelled through a Gaussian filtering process. Applying Gaussian filtering to an image reduces the amount of high frequencies observable in the image. It is tempting to say, "high detailed images are less sparse than low detailed images". This statement can easily be disproved by creating an image with a single 2-dimensional high-frequency sine-wave. In the Fourier domain such a signal will only require two coefficients. Applying a Gaussian filter to the same image will increase the required Fourier coefficients to represent the new image.

Optical images taken from a natural scene is not sparse and thus by adding the assumption that the image is of a natural scene, one can comment that a high detailed image is less sparse.

A focal-plane array can be simulated by using a large image, applying an appropriate Gaussian filter followed by area averaging (downsampling) to measure the intensity of each pixel. From the previous section we showed how the PSNR changed over the sparsity of an image here the same sparsity effects can be observed through Gaussian filtering and down sampling of images and is shown in Figure 12. It is observed that higher filtering and down sampling require less coefficients to reconstruct the complete image. Using the sparsity measure and PSNR values we can estimate the performance of a rosette imager by the size of a focal-plane array.
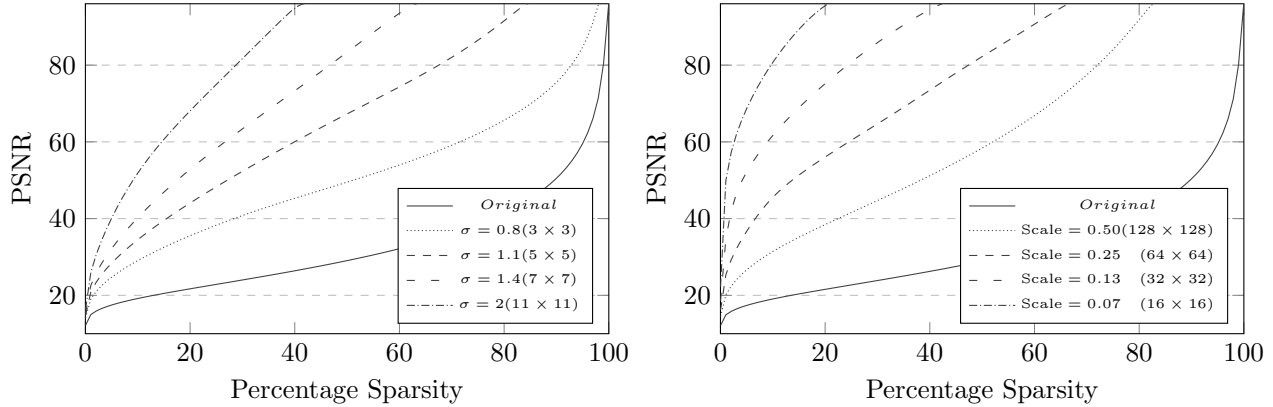
(a) Gaussian Filtering versus image sparsity (b) focal-plane array versus Image sparsity

Figure 12: Two graphs indicating how reducing the expected SFR influence the image sparsity. A lower expected SFR produces a sparser natural image in the Discrete Cosine Transform basis.

3.4 Experimental Protocol

We conducted two experiments in order to assess the performance of the Rosetta Imager. The experiments use group comparison through Bayesian Estimation as presented by Kruschke.[20] From Section 3.3 the PSNR distributions validate the usage of a student t-distribution for the model approximation and with no previous results, the priors are taken as uniform (See Appendix A.3).

Rather than using p-values or confidence interval for evaluating the null hypothesis of effect size, we instead use Bayesian estimation with a Highest Density Interval of 95% measured on the effect size. Thus the relative performance of two algorithms are evaluated by approximating the posterior distribution of the effect size via Markov Chain Monte Carlo (MCMC). Typically negative effect size values support the first algorithm and a positive effect size values suppor the second algorithm. However from a Bayesian perspective the algorithm is assumed to perform better if the 95% Highest Density Interval (HDI) of the effect size are strictly positive.

The first experiment evaluate the optimal rosette pattern for limiting rotational frequency of 2500 Hz against three other possible patterns. The first pattern, (11, 4) is a previously published pattern, although the purpose of this pattern was only to demonstrate image formation using a rosette scanner and compressed sensing. The second pattern is selected by limiting the maximum rotational frequency to 1000 Hz. The third pattern, (56, 99), was randomly selected from the top 10 patterns found through the optimisation process. Each pattern is used on both data sets outputting a set of PSNR values with related averages and standard deviations. These outputs are then used to perform Bayesian estimation.

The second experiment compare the performance of a focal-plane array (FPA) to the optimal rosette pattern. The focal-plane array is simulated by down sampling the image to the appropriate size, followed with a linear up scaling to allow for equivalent PSNR measurements. The experiment is only performed using the dead leaves data set. Comparing a single sized FPA to the optimal rosette pattern would not provide any insight and therefore a range of FPA sizes are tested. Using the effect size and the 95% HDI the expected probability that an image from the FPA will be better than the rosette imager can be estimated.

4. RESULTS

4.1 Scanning Pattern Results

The results of the four patterns are shown in Table 3 with example images in Figure 13.

Table 3: rosette imager pattern evaluation results

Pattern (n, m)	Frequency 1 (Hz)	Frequency 2 (Hz)	Probe Size (pixels)	Dead leaves (Average PSNR)	Natural Scene (Average PSNR)
(11 4)	100	-175	31	13.63(1.05)	20.22(2.84)
(76 37)	925	-975	2.25	17.36(1.19)	25.58(3.76)
(56 99)	2475	1075	2.25	17.67(1.25)	25.90(3.86)
(8 99)	2425	2275	2.25	17.67(1.24)	26.00(3.90)

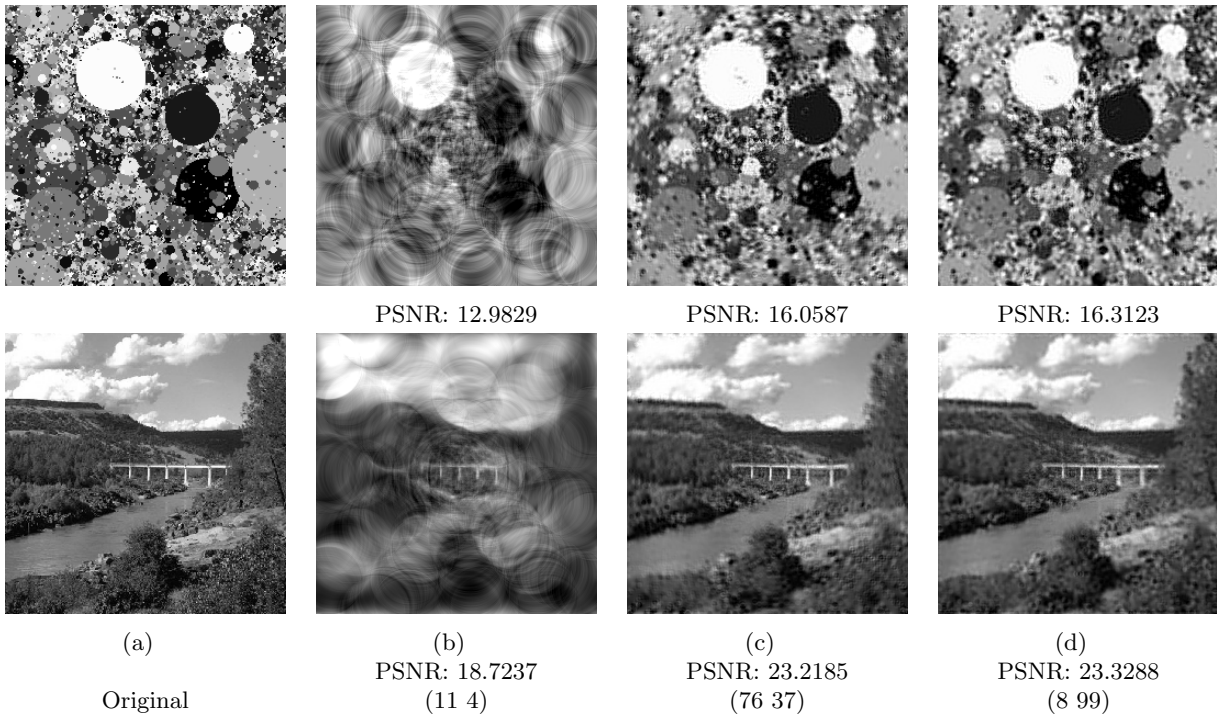|	PSNR: 12.9829	PSNR: 16.0587	PSNR: 16.3123
(a)	(b)	(c)	(d)
	PSNR: 18.7237	PSNR: 23.2185	PSNR: 23.3288
Original	(11 4)	(76 37)	(8 99)

Figure 13: Example images generated by using the various scanning patterns.

First (11 4) and (8 99) is compared. A comparison between averages in PSNR show that (8, 99) outperform (11 4) on both data sets and the difference far exceeds the standard deviations. An example comparison between the two patterns can be made visually in Figure 13b and Figure 13d.

The second evaluation is between (8 99) pattern and (76 37) pattern. Comparing the means of the PSNR of each data set, (8 99) is better than (76 37) although the standard deviations are large compared to the difference in means. A visual inspection can be performed between Figure 13c and Figure 13d and only slight degradation's can be observed between the dead leaves patterns. This difference might only be specific to the image example. To dig deeper in the comparison the Bayesian estimation is shown in Figure 14.
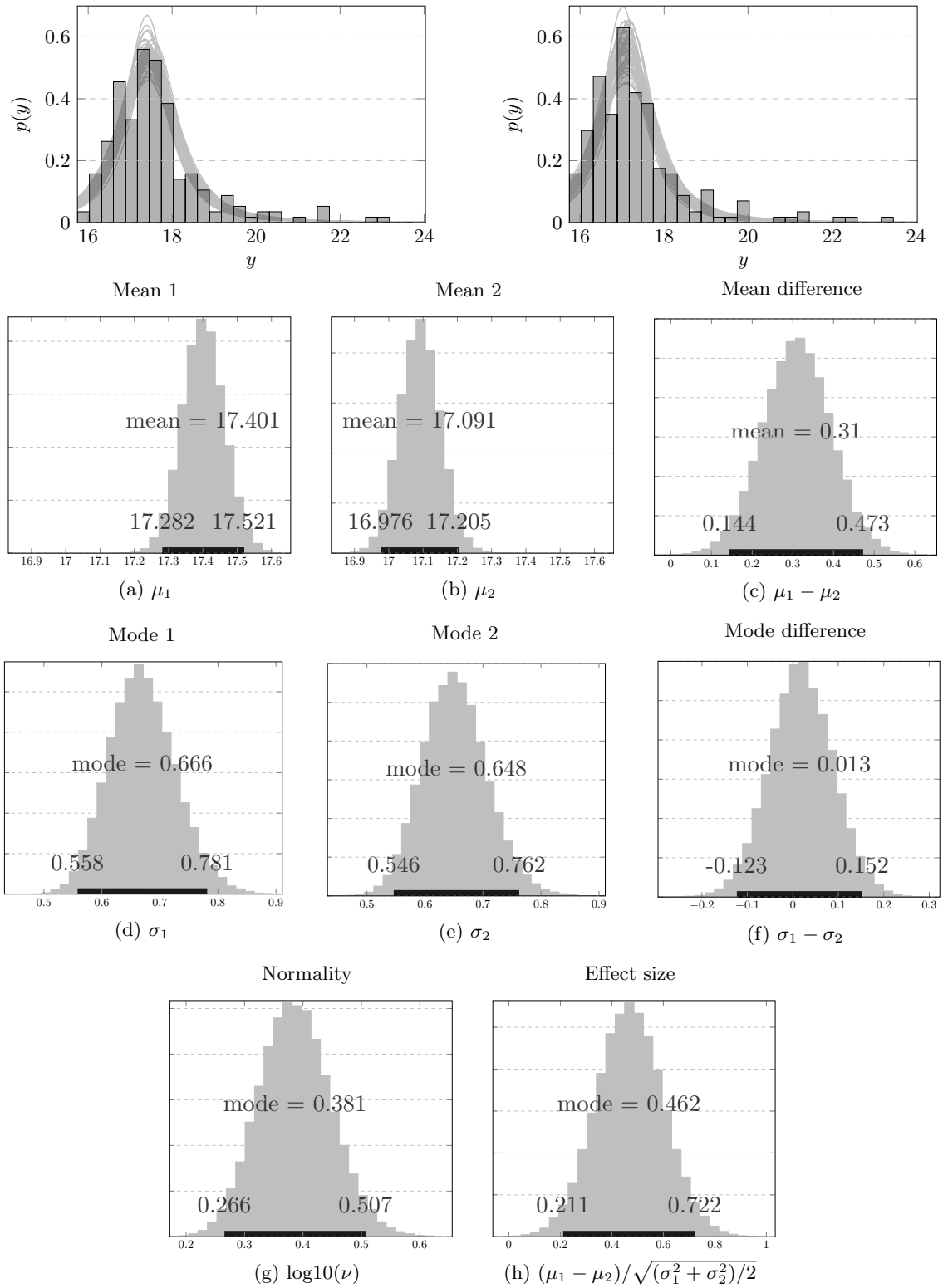
Figure 14: The results of the Bayesian estimation between (76 37) and (8 99). The 95% HDI of the effect size indicate that (8 99) is statistically better than (76 37).

In the first row of the figure the estimated posterior probability distribution of the PSNR values are overlaid with the histogram data of the sampled data. The second row show the posterior distributions for the μ parameter and the difference of means indicate that the difference are statistically significant. It is interesting to note how these means differ from the averages shown in Table 3. If the data is roughly symmetric, the comparison of the μ parameter can be adequate. The third row provide the mode or somewhat the data variance. The difference in modes according to the 95% HDI is not significant. The lower left graph provide the distribution of the normality parameter, where small values indicate large tailed distributions. The posterior distribution is relatively narrow indicating the consistent accommodation of outliers within the data. The last posterior distribution show the credible effect size of the two data groups. The 95% HDI of the effect size supports the hypothesis that group 2 is significantly higher than group 1. The Bayesian estimation shows that the 95% HDI of the effect size is not shared between the two patterns and therefore it is expected that (8 99) performs better than the (76 37) pattern.

The third evaluation, between (8 99) pattern and (56 99) pattern, is somewhat more tricky. Evaluating the PSNR averages (8 99) performs equivalent to that of (56 99) on the dead leaves pattern but much better on the natural data set. A Bayesian estimation is performed on the dead leaves data set and the natural scene data set with only the output of the effect sizes shown in Figure 15. Taking the 95% HDI, the difference in performance is not statistical significant and we can therefore not say that the one pattern is better than the other.

Effect size for dead leaves pattern   Effect size for natural pattern

mode = 0.000379   mode = 0.0185

-0.246   0.247   -0.03   0.077

(a) $(\mu_1 - \mu_2)/\sqrt{(\sigma_1^2 + \sigma_2^2)/2}$ (b) $(\mu_1 - \mu_2)/\sqrt{(\sigma_1^2 + \sigma_2^2)/2}$
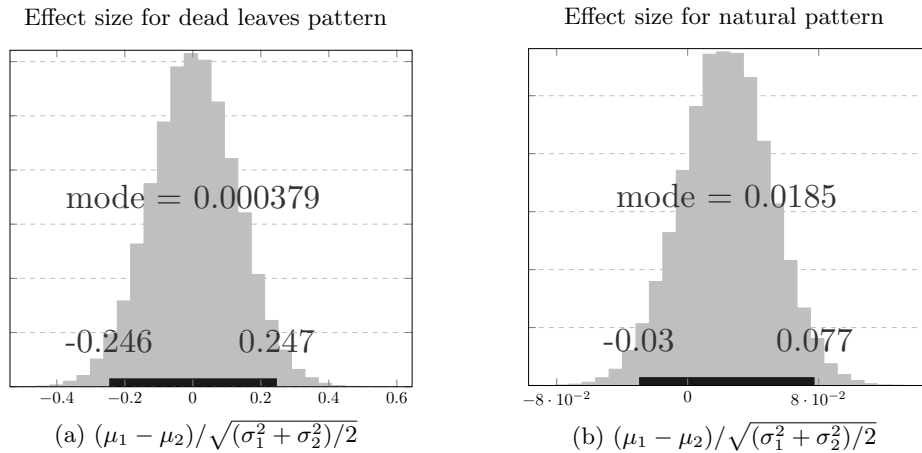
Figure 15: The effect sizes of Bayesian estimation between (56 99) and (8 99) on the dead leaves data set and natural scene data set. The 95% HDI indicate that there is no significant difference between the two patterns.

4.2 Focal-plane Array Comparison Results

The results for comparing the range of focal-plane arrays to the (8 99) pattern is shown in Figure 16. It can be seen from the graph that an FPA of size 114×114 will only produce an image 30% of the time with a higher PSNR value than the rosette imager. From the analysis the rosette imager will produce an image 95% of the time equivalent to a 111×111 up to 121×121 FPA. Uniformly sampling the imaging area 12974 samples can be used in image reconstruction and thus an FPA with equivalent number of samples rounded up would be a 114×114 FPA.
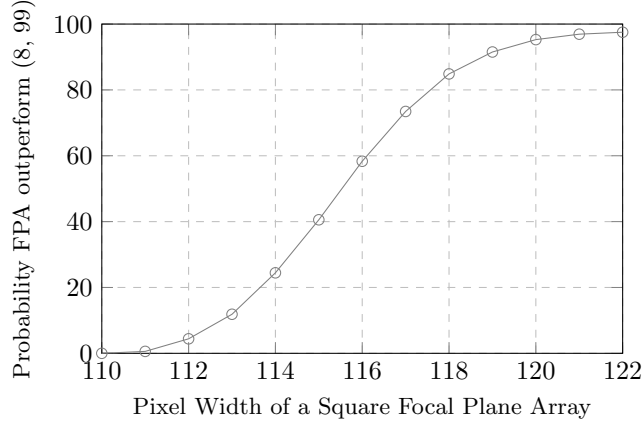
Figure 16: The probability according to the 95% HDI that the specific sized FPA will outperform the rosette imager on a sampled image.

5. DISCUSSION

The designed rosette imager is based on a rosette scanner and the Fourier Domain Regularisation Inversion algorithm. The imager use a single sensor with an instantaneous field of view equal to 2.25 pixels; It samples at 510 kHz to output a 256×256 image at 25 frames per second. Furthermore, the wedge rotates at 2475Hz, and the mirror rotates at 2275 Hz. The set-up produced images of equivalent quality as focal-plane arrays of size 111×111 to 121×121.

We expected that the rosette imager would perform just as well as the focal-plane array. The performance is due to the signal sparsity requirement in compressed sensing theory. In the exploration of image sparsity we have also shown that natural images are not sparse. The development of an imager using a single detector scanning system compared to a focal-plane array allow for different trade-offs (such as image quality versus number of samples needed). Further modelling of a rosette imager will better establish these trade-off parameters. We note that the same rosette pattern can be achieved by replacing the rosette scanner with a Risley prism.

The image sparsity investigation highlighted the effect of different image categories on the expected PSNR and image sparsity itself. Furthermore, the investigation indicates that the performance of algorithms are dependant on the set of testing images. Preferably algorithms should be compared using the same set of images. It is also suggested that using only the dead leaves pattern for comparison should be adequate for a large range of algorithms in image formation. The PSNR measure and image sparsity was shown to provide estimates of the spatial frequency response of the imager. These measurements can likely assist evaluations in the laboratory. Finally, we note that advanced statistical techniques such as Bayesian estimation will benefit the evaluation of image formation and image processing algorithms.

APPENDIX A. EQUATIONS

A.1 Rosette scanner governing equations

The wedge typed device can be described by the following design equations:[8]

$$\phi_2 \approx \frac{\phi_1(n-1)d_1}{2d_2}$$

with ϕ_1 the vertical angle of the wedge, ϕ_2 the canted angle of the secondary mirror, n is the refractive index of the wedge, d_1 is the distance of wedge from the sensor and d_2 is the distance of the mirror from the sensor. The locus of the IFOV is given by:

$$x = \phi_2 \left(\cos(2\pi f_1 t) - \cos(2\pi f_2 t) \right)$$
$$y = \phi_2 \left(\sin(2\pi f_1 t) - \sin(2\pi f_2 t) \right)$$

Furthermore, it is required that the rosette scanning pattern is repeated at a specified time interval T; which also relate to the specified frame rate of the imager $1/T$. The frame rate in conjunction with rotating elements are constrained by:

$$T = \frac{m}{f_1} = \frac{m-n}{f_2} = \frac{n}{f_1 - f_2}$$

with $n, m \in \mathbb{Z}$.

A.2 Peak-Signal to Noise Ratio Equations

Given an image I of height H and width W such that $I(m,n) \mapsto i_{m,n} \in 0, \ldots, 2^{16} - 1$ with $|m| \leq H - 1$, $|n| \leq W - 1$ and $m, n \in \mathbb{Z}$. The Mean Square Error between a reference image I_R and a test image I_T is given be

$$MSE(I_T, I_R) = \frac{1}{HW} \sum_{m=0}^{H-1} \sum_{n=0}^{W-1} [I_T(m,n) - I_R(m,n)]^2$$

The Peak Signal-to-Noise Ratio (PSNR) in decibel (dB) is defined as

$$PSNR(I_T, I_R) = \begin{cases} 20 \cdot \log_{10}\left(\frac{2^B - 1}{\sqrt{MSE(I_T, I_R)}}\right) & MSE(I_T, I_R) \geq 1 \\ 20 \cdot \log_{10}\left(2^B - 1\right) & Otherwise \end{cases} \tag{1}$$

A.3 Student t-distribution

The student t-distribution is given by

$$\text{StudentT}(y|\nu, \mu, \sigma) = \frac{\Gamma\left((\nu+1)/2\right)}{\Gamma(\nu/2)} \frac{1}{\sqrt{\nu\pi}\,\sigma} \left(1 + \frac{1}{\nu}\left(\frac{y-\mu}{\sigma}\right)^2\right)^{-(\nu+1)/2}$$

with ν as the normality parameter, μ as the mean, σ as standard deviation and y as the data point.

The effect size is calculated by:

$$\text{Effect Size} = \frac{(\mu_1 - \mu_2)}{\sqrt{\frac{1}{2}\left(\sigma_1^2 + \sigma_2^2\right)}}$$

REFERENCES

[1] Kinch, M., [*State-of-the-art infrared detector technology*], SPIE (January 2014).

[2] Donoho, D. L., "Compressed sensing," *IEEE Transactions on information theory* **52**(4), 1289–1306 (2006).

[3] Uzeler, H., Cakir, S., and Aytaç, T., "Image generation for single detector infrared seekers via compressive sensing," *Proceedings of SPIE - The International Society for Optical Engineering* **8896** (2013).

[4] Uzeler, H., Cakir, S., and Aytaç, T., "Compressive sensing applications for single detector rosette scanning infrared seekers," *Electro-Optical and Infrared Systems: Technology and Applications XII; and Quantum Information Science and Technology* **9648**(October 2015) (2015).

[5] Uzeler, H., Cakir, S., and Aytaç, T., "Image reconstruction for single detector rosette scanning systems based on compressive sensing theory," *Optical Engineering* **55**(2) (2016).

[6] Jiang, Y., Tong, Q., Wang, H., Yang, Z., and Ji, Q., "Image recovery of an infrared sub-imaging system based on compressed sensing," *Symmetry* **9**(11) (2017).

[7] Tong, Q., Jiang, Y., Wang, H., and Guo, L., "Image reconstruction of dynamic infrared single-pixel imaging system," *Optics Communications* **410** (2018).

[8] Tajime, T and Wakabavashi, S and Kondo, M and Takei, T., "Rosette Scan Infrared Sensor," *Electro-Optical Technology for Autonomous Vehicles* **219**(April 1980), 51–57 (1980).

[9] Foucart, S. and Rauhut, H., [*A Mathematical Introduction to Compressive Sensing*], Applied and Numerical Harmonic Analysis, Springer New York (2013).

[10] van den Berg, E. and Friedlander, M. P., "Probing the pareto frontier for basis pursuit solutions," *SIAM Journal on Scientific Computing* **31**(2), 890–912 (2008).

[11] Czajkowski, K. M., Pastuszczak, A., and Kotyński, R., "Real-time single-pixel video imaging with fourier domain regularization," *Opt. Express* **26**, 20009–20022 (Aug 2018).

[12] Lee, A. B., Mumford, D., and Huang, J., "Occlusion models for natural images: A statistical study of a scale-invariant dead leaves model," *International Journal of Computer Vision* **41**(1-2), 35–59 (2001).

[13] Gousseau, Y. and Roueff, F., "The dead leaves model: general results and limits at small scales," *arXiv preprint math/0312035* **0**, 1–38 (2003).

[14] Kendall, W. S. and Thönnes, E., "Perfect simulation in stochastic geometry," *Pattern Recognition* **32**(9), 1569–1586 (1999).

[15] Oliva, A. and Torralba, A., "Modeling the shape of the scene: A holistic representation of the spatial envelope," *International journal of computer vision* **42**(3), 145–175 (2001).

[16] Z. Wang, A. C. Bovik, H. R. S. and Simoncelli, E. P., "Image quality assessment: From error visibility to structural similarity," *IEEE Transactions on Image Processing* **13**(4), 600–612 (2004).

[17] Horé, A. and Ziou, D., "Image quality metrics: PSNR vs. SSIM," *Proceedings - International Conference on Pattern Recognition* **1**, 2366–2369 (2010).

[18] Dosselmann, R. and Yang, X. D., "A comprehensive assessment of the structural similarity index," *Signal, Image and Video Processing* **5**(1), 81–91 (2011).

[19] Brunet, D., Vrscay, E. R., and Wang, Z., "On the mathematical properties of the structural similarity index," *IEEE Transactions on Image Processing* **21**(4), 1488–1495 (2012).

[20] Kruschke, J. K., "Bayesian estimation supersedes the T test," *Journal of Experimental Psychology: General* **142**(2), 573–588 (2013).